Supporting Information

Mutual Suppression of Mn_3O_4 and SiO_x in an Innovative Anode Design for Enhanced Cycling Stability

Miao Li, Quan Ouyang, Kai Yao, Yaowen Wang, Mingwei Ma, Shilong Fu, Xu Zhao, Guangshe Li*, Liping Li*

State Key Laboratory of Inorganic Synthesis and Preparative Chemistry, College of Chemistry, Jilin University, Changchun, 130026, P.R. China

*Corresponding authors.

E-mail addresses: lipingli@jlu.edu.cn; guangshe@jlu.edu.cn

1   Experimental section

1.1   Chemicals

(3-Aminopropyl)trimethoxysilane (APTMS), cetyltrimethylammonium bromide (CTAB, 99%) were purchased from Aladdin Reagent. Tetraethyl orthosilicate (TEOS), resorcinol($\geq$99.5%), formaldehyde solution (37-40%), ammonia solution ($NH_3 \cdot H_2O$，25-28%)，ethanol ($\geq$99.7%) were purchased from Sinopharm Reagent. $KMnO_4$ was purchased from Beijing Institute of Chemical Reagents. All the chemicals were used without further purification.

1.2   Preparation of SiO_x@C/Mn_3O_4

1.2.1   Synthesis of Ultrafine SiO_x Nanoparticles

0.3 g CTAB was dissolved in a mixed solution of 45 mL ethanol and 75 mL water, followed by the addition of 1 mL concentrated $NH_3 \cdot H_2O$. The resulting mixture was stirred in a 35 °C water bath for 10 min. Subsequently, a mixture of 1 mL TEOS and 1 mL APTMS as the silicon source was rapidly added to the aforementioned solution, which was then stirred at 35 °C for 24 h. The precipitate was collected through centrifugation and washed several times with deionized water and ethanol, followed by drying overnight to obtain the white product SiO_x. The SEM image of SiO_x is shown in Figure S1a.

1.2.2   Synthesis of SiO_x@C nanoparticles

0.2 g as-prepared SiO_x was added to a mixed solution of 12 mL ethanol and 30 mL water. Subsequently, 0.23 g CTAB, 0.07 g resorcinol, and 0.1 mL $NH_3 \cdot H_2O$ were added in sequence, and the mixture was stirred in a 35 °C water bath for 0.5 h. Then, 0.1 mL formaldehyde was added dropwise, and the reaction continued in the water bath for 6 h, followed by aging at room temperature for 12 h. Finally, the precipitate was collected by centrifugation, washed several times with deionized water and ethanol, and dried overnight to obtain the orange product SiO_x@RF. The dried SiO_x@RF was then calcined at 800 °C in a 10% H_2/Ar atmosphere for 3 h to obtain a black powder SiO_x@C.

The SEM images of SiO_x@RF and SiO_x@C are shown in Figure S1b, S1c.

1.2.3 Synthesis of SiO_x@C/Mn_3O_4

The above 0.12 g SiO_x@C was added to $KMnO_4$ (0.01 M, 0.02 M, 0.03 M) solutions with different concentrations, and kept in a water bath at 70 °C for 2 h. The precipitate was then collected by filtration and washed several times with water and ethanol, and dried overnight. The dried product was calcined at 300 °C in a 10% H_2/Ar atmosphere for 5 h to obtain products with different silicon-manganese ratios. These products were designated as SCM-1, SCM-2, and SCM-3, respectively. The SEM image of SiO_x@C/MnO_2 (the precursor of SCM-2) is shown in Figure S1d.

1.3 Material Characterization

Scanning electron microscopy (SEM; JEOL, model JSM-6700F), transmission electron microscopy (TEM; Tecnai G2 S-Twin F20) and high-resolution TEM (HRTEM) were used to characterize the morphology and structure of all samples. Energy-dispersive X-ray spectroscopy (EDS) was performed using an Oxford X-Max80 instrument. X-ray diffraction (XRD) analysis was conducted utilizing a Rigaku D/max-2550 diffractometer with Cu Ka radiation to ascertain the crystalline and amorphous composition of the specimens. A INVIA Confocal Raman spectrometer was used to collect Raman spectra at a wavelength of 488 nm in the range of 1000-2000 cm^{-1} to analyze the graphitization degree of the specimens. Fourier transform infrared (FT-IR) spectra was obtained utilizing a Bruker VERTEXV 80V spectrophotometer equipped with a Platinum-ATR A225/Q accessory (Bruker). The chemical bonds and valence states of elements were examined through X-ray photoelectron spectroscopy (XPS) using Al Kα as the X-ray source with an ESCA-LAB250 instrument. All the spectra were calibrated based on the C 1s peak at 284.8 eV.

1.4 Electrochemical characterization

The as-prepared SCM was mixed with conductive agent (Super P) and sodium

alginate in a mass ratio of 70:15:15 and dissolved in deionized water to form a uniform slurry. The slurry was then coated onto copper foil using a scraper and vacuum-dried at 80 °C for 12 h. After drying, the copper foil was cut into disks with a diameter of 14 mm, and the average mass loading of the active material was 0.7 mg cm^{-2}. The CR2025 half-cells were assembled in an argon-filled glove box with water and oxygen content less than 0.1 ppm. The lithium metal foil was used as counter electrode and Celgard 2500 as the separator. The electrolyte consisted of 1 M LiPF$_6$ dissolved in a mixture of ethylene carbonate (EC) and dimethyl carbonate (DMC) in a 1:1 volume ratio, with 5.0 vol% fluoroethylene carbonate (FEC) as an additive. The assembled half-cells were tested on a Neware battery test system. Cyclic voltammetry (CV) measurements were performed using a CHI 660E electrochemical workstation at a scan rate of 0.2 mV s^{-1} within a voltage window of 0.01-3.0 V. Galvanostatic Intermittent Titration Technique (GITT) measurements were conducted using the Neware battery test system (conducted at 0.1 A g^{-1}, with a pulse time of 10 min and a relaxation time of 2 h). Prior to the experiment, the half-cell was pre-cycled at 0.1 A g^{-1} for one cycle to eliminate the impact of the solid electrolyte interphase (SEI) on D_{Li+}. *In-situ* EIS was tested at afrequency range from 100 mHz to 100 kHz on electrochemical workstation (Squidstat Plus).
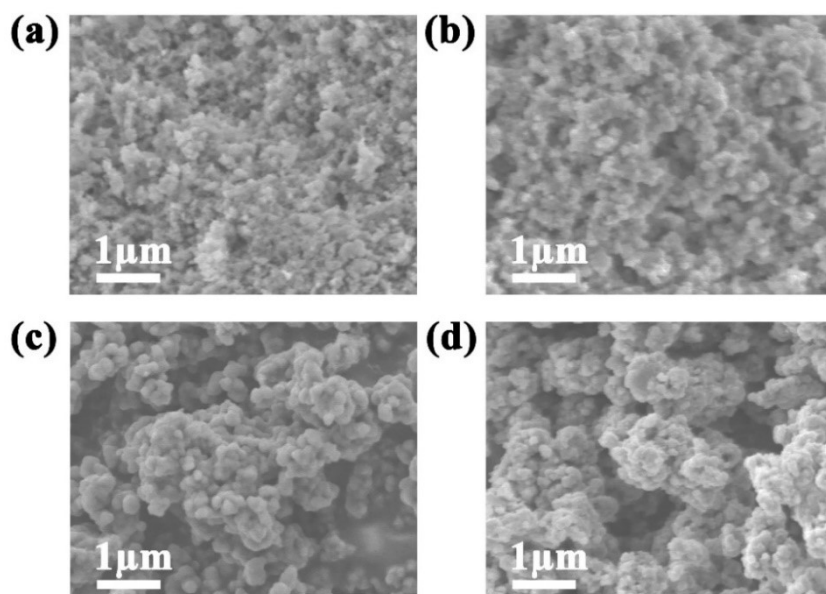
Fig. S1. SEM images of (a)SiO$_x$, (b) SiO$_x$@RF, (c) SiO$_x$@C and (d) SiO$_x$@C/MnO$_2$ (the precursor of SCM-2).
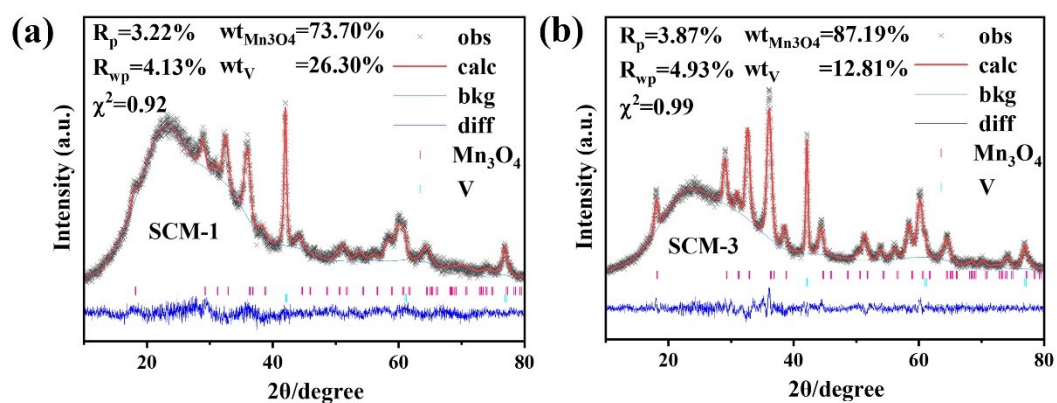

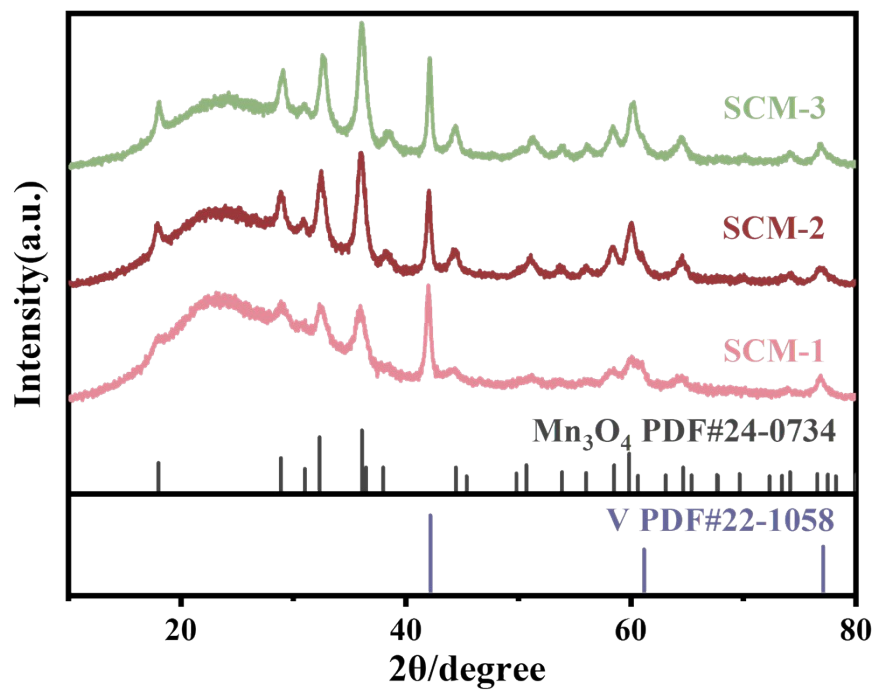Fig. S2. XRD refinement results of (a) SCM-1 and (b) SCM-3.

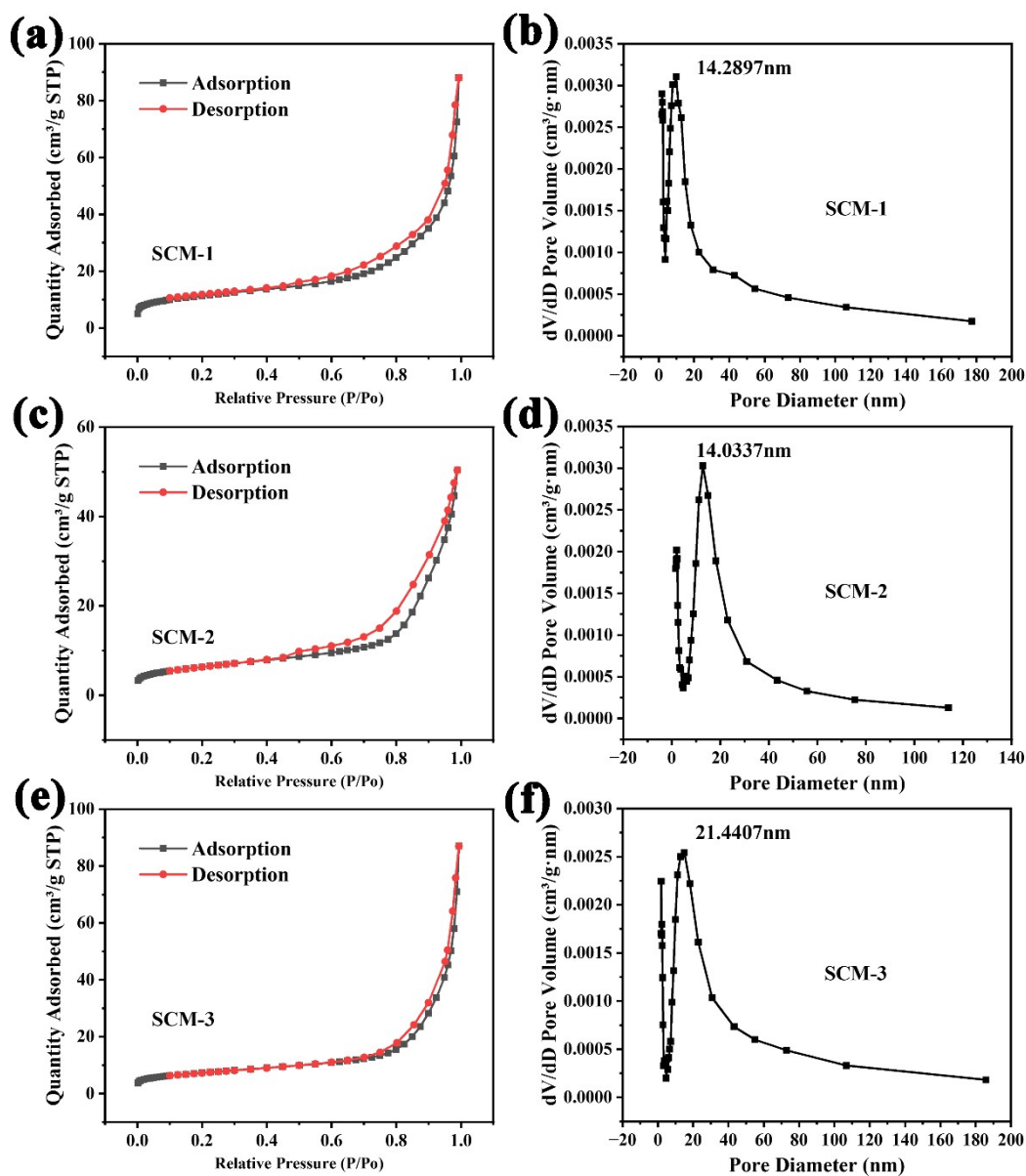Fig. S3. Comparison of XRD patterns of three SCM samples.

Fig. S4. N$_2$ adsorption/desorption curves and pore size distribution curves of (a, b) SCM-1, (c, d) SCM-2 and (e, f) SCM-3.
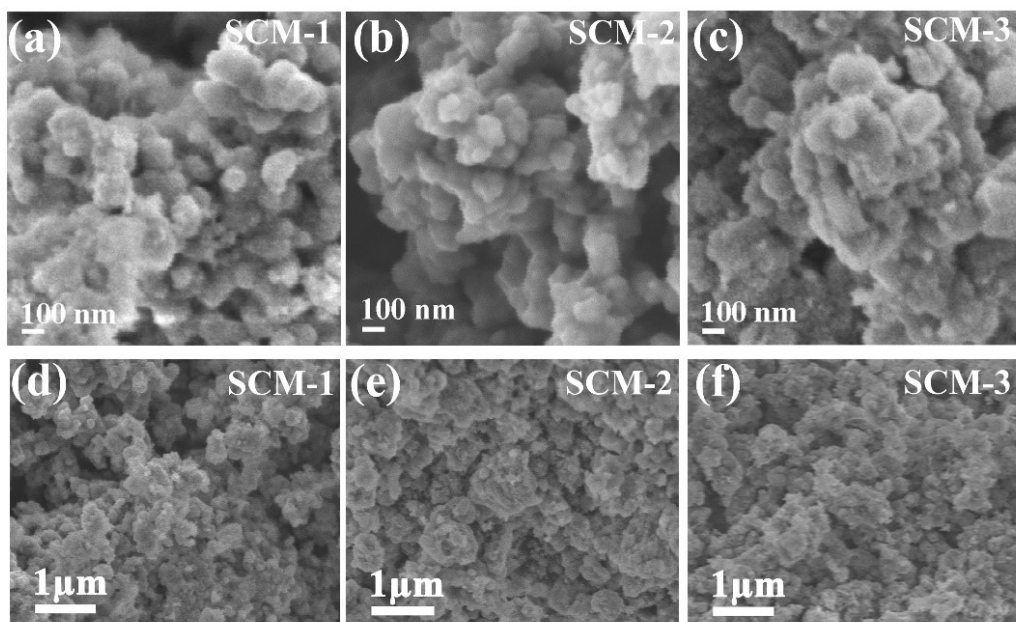
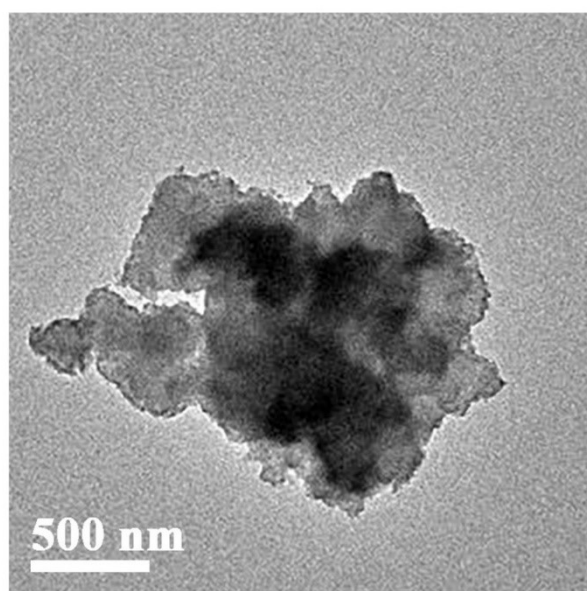Fig. S5. (a-f) SEM images of SCM-1, SCM-2, and SCM-3.
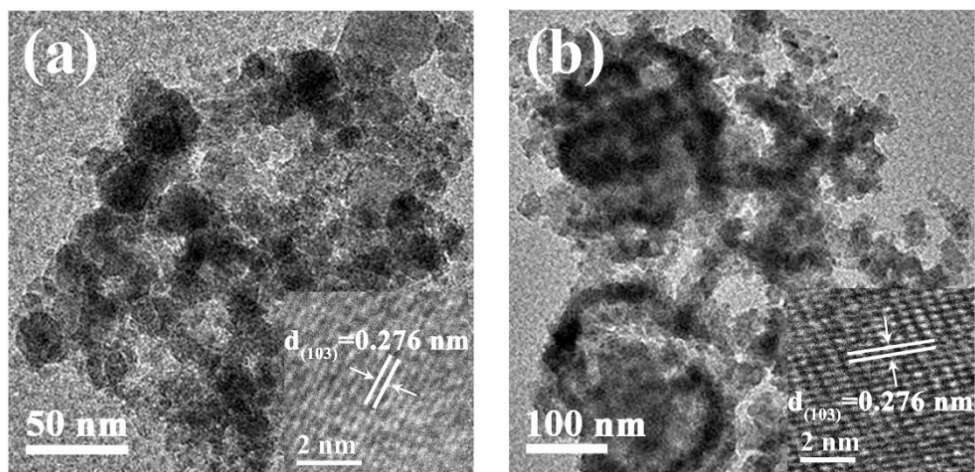

Fig. S6. TEM images of SCM-2.

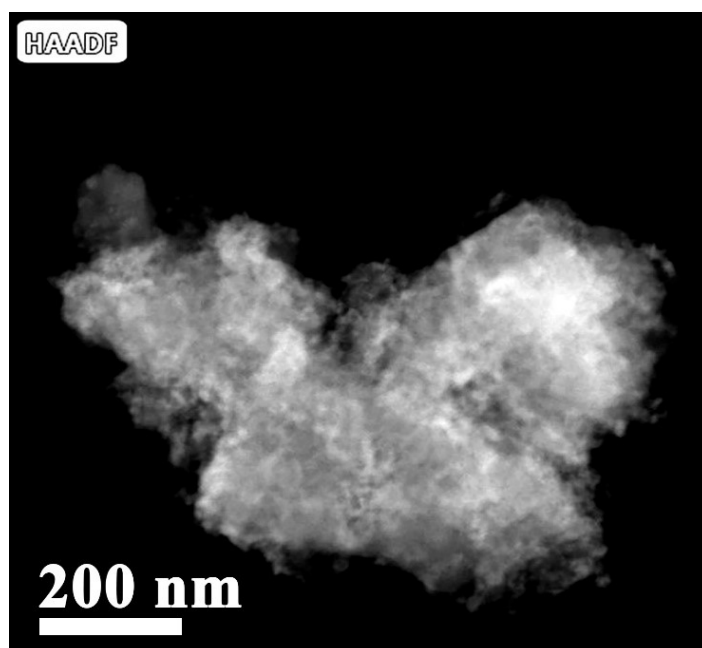Fig. S7. (a, b) TEM and HRTEM images of SCM-1 and SCM-3

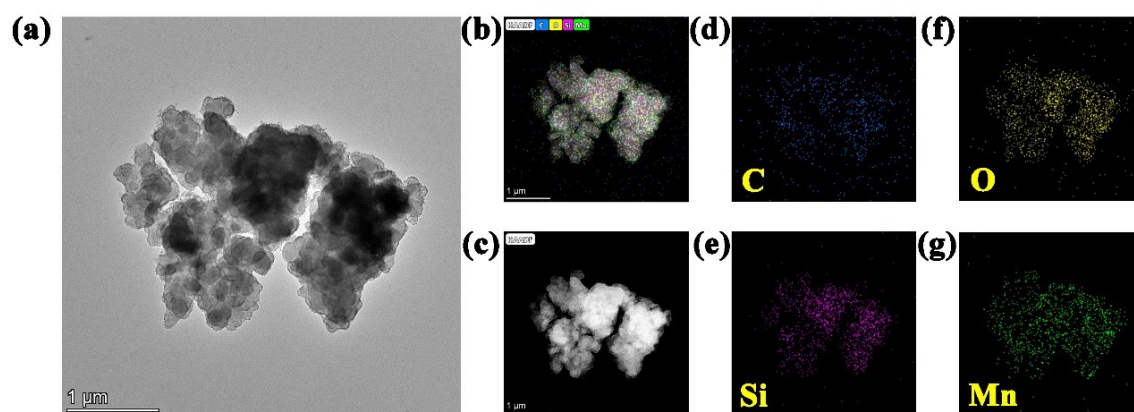Fig. S8. High-angle annular dark field (HAADF) image of SCM-2.

Fig. S9. High-angle annular dark field (HAADF) images and the corresponding EDS elements distribution mappings of SCM-1.
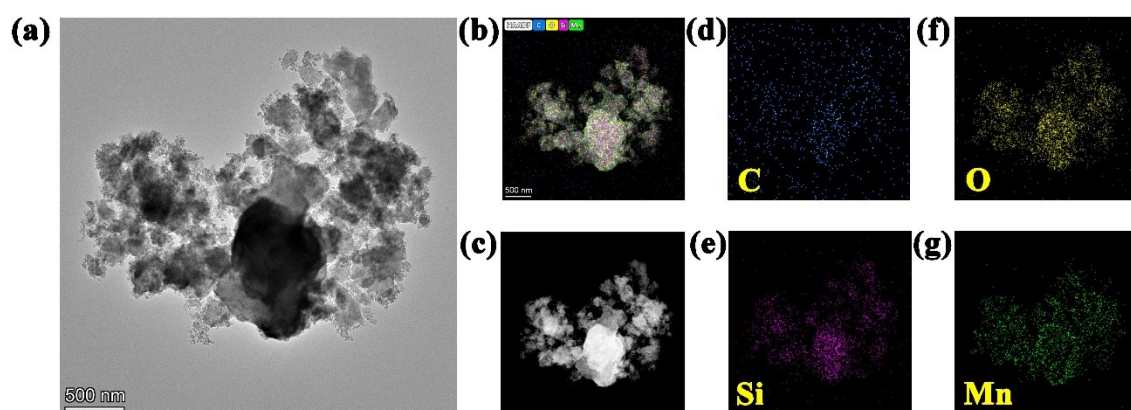

Fig. S10. High-angle annular dark field (HAADF) images and the corresponding EDS elements distribution mappings of SCM-3.
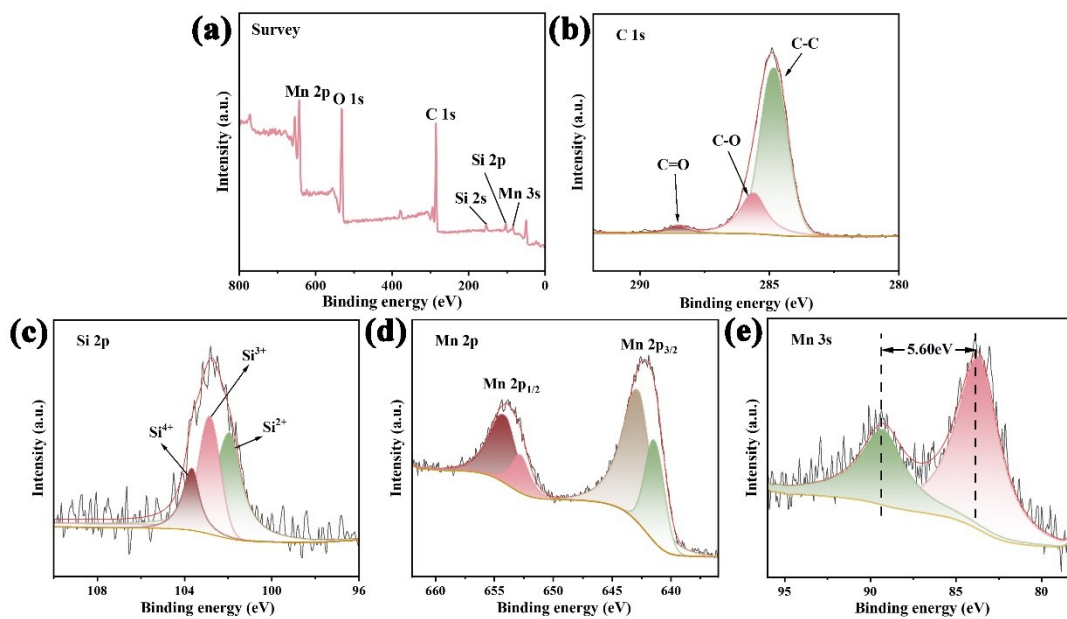
Fig. S11. (a) XPS survey spectrum, (b) C 1s, (c) Si 2p, (d) Mn 2p and (e) Mn 3s of SCM-2.
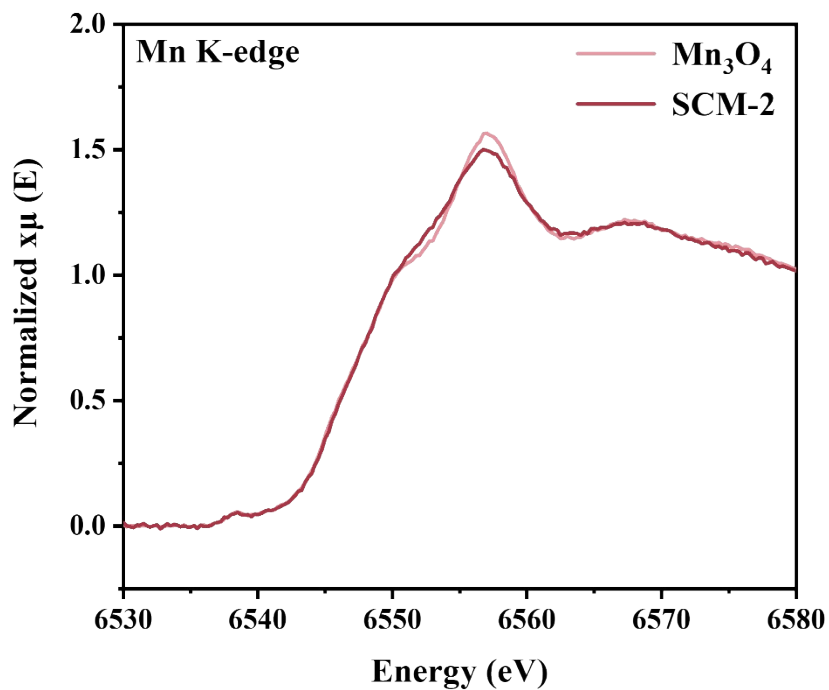
Fig. S12. Normalized Mn K-edge XANES spectra of SCM-2 and Mn_3O_4.
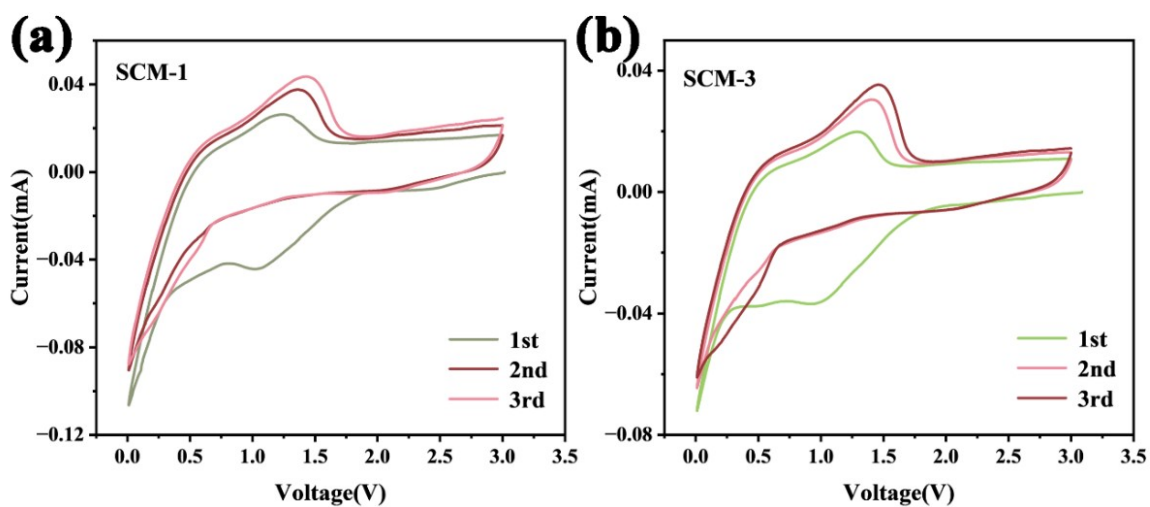
Fig. S13. Cyclic voltammetry curves of (a) SCM-1 and (b) SCM-3 at a scan rate of 0.2 mV s^{-1} for the initial three cycles.

Fig. S14. dQ/dV curves of (a) SCM-1 and (b) SCM-3.

Fig. S15. Capacity-voltage curves of (a) SCM-1 and (b) SCM-3.
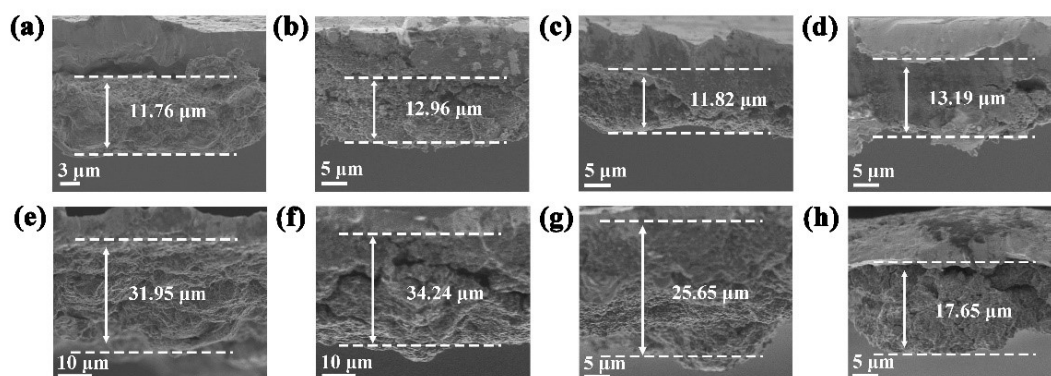
Fig. S16. Cross-sectional SEM images of (a and e) Mn_3O_4, (b and f) SiO_x, (c and g) $SiO_x@C$ and (j and h) SCM-2 electrodes before and after 5 cycles.

Table S1. Comparison of electrochemical performance of various Mn_3O_4-based electrodes

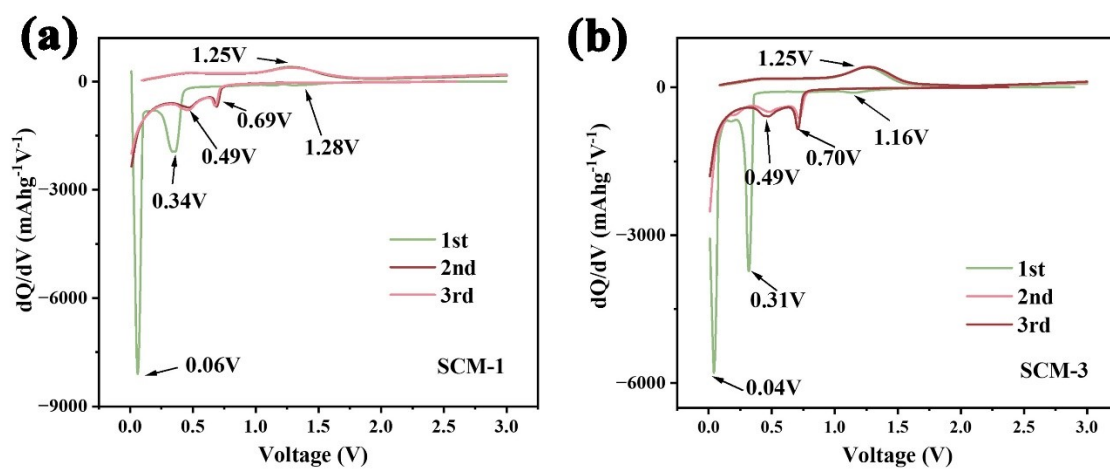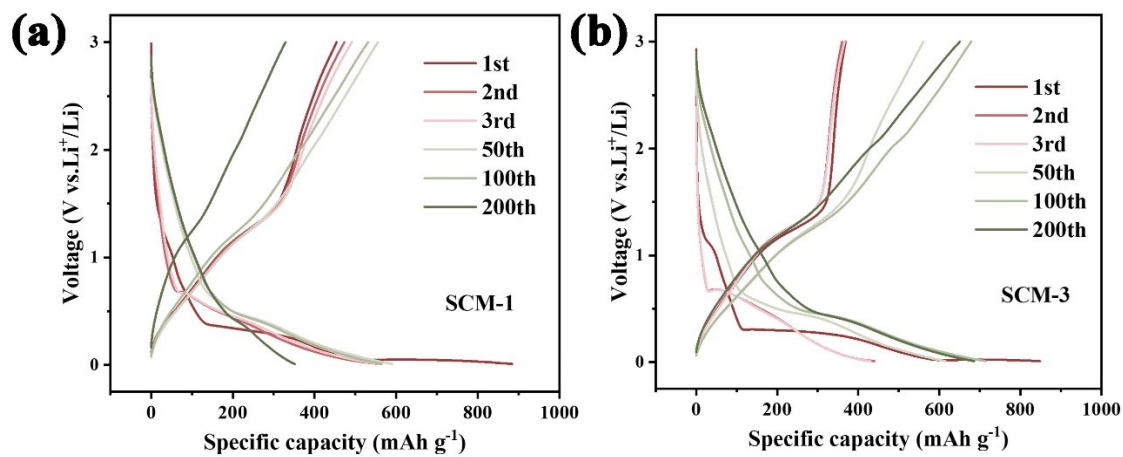| Materials	Current density (A g^{-1})	Cycle number	Capacity (mAh g^{-1})	Ref.
Mn_3O_4 nanowires	0.2	100	400	1
Mn_3O_4@C	0.25	200	730.2	2
$MnCO_3$@ Mn_3O_4@rGO	0.1	200	988	3
Mn_3O_4@CNT/TiO_2	0.2	100	880	4
rGO/Mn_3O_4 nanocomposite	0.1	100	702	5
HCF/ Mn_3O_4	0.2	100	835	6
AC-PCAH/N/Mn_3O_4	0.1	120	806	7
MKAC-180	0.2	100	838.1	8
rGO/Mn_3O_4	0.1	200	798.5	9
ArGO/Mn_3O_4 NR	0.2	100	749	10
SiO_x@C/Mn_3O_4	0.2	200	862.44	This work

Compared with most Mn_3O_4-based materials reported in the literature, the specific capacity of SiO_x@C/Mn_3O_4 at low current density is in the upper-middle range (Table S1 in the Supporting Information).

Table S2. Contents of SiO_x and Mn_3O_4 in three SCM samples and the refinement results of XRD patterns.

Sample	$m_{SCM}:m_V$	$wt_{amorphous\ phase}$ (%)	wt_{Mn3O4} (%)	R_p (%)	R_{wp} (%)	χ^2
SCM-1	10:1	71.98	28.02	3.22	4.13	0.92
SCM-2	10:1	40.60	59.40	3.50	4.49	0.90
SCM-3	10:1	31.94	68.06	3.87	4.93	0.99

Table S3. Carbon content obtained by CHNS element analysis for three SCM samples.

Sample	Weight (mg)	C (%)
SCM-1	1.8900	17.78
SCM-2	2.2520	11.66
SCM-3	2.0270	5.64

Supplementary Note 1 The lithium storage mechanism of SCM anode materials.

Taking SCM-2 as an example, the broad peak at 1.28 V during the first discharge process corresponds to the irreversible transformation of SiO_x with metallic Li to form lithium silicate and crystalline silicon. The sharp peak at 0.33 V corresponds to the generation of MnO from Mn_3O_4, while the sharp peak at 0.07 V can be attributed to the reduction of MnO to metallic Mn and the lithiation process of crystalline silicon. In subsequent cycles, the cathodic peaks observed at 0.51 V and 0.7 V were found to shift towards higher potentials. This shift can be attributed to the diminished polarization resulting from enhanced reaction kinetics after initial lithiation process. Moreover, the cathodic peak observed at 0.51 V also includes the lithiation process of amorphous silicon generated after the first cycle. In brief, the lithium storage mechanism of SCM anode materials can be elucidated by the subsequent formula (eq1-5):

$$Mn_3O_4+8Li^++8e^-\leftrightarrow3Mn+Li_2O \tag{1}$$

$$SiO_x+2xLi^++2xe^-\rightarrow xLi_2O+Si \tag{2}$$

$$5SiO_x+2xLi^++2xe^-\leftrightarrow Li_2Si_2O_5+(5-2x)\ Si \tag{3}$$

$$4SiO_x+4xLi^++4xe^-\rightarrow xLi_4SiO_4+(4-x)\ Si \tag{4}$$

$$Si+xLi^++xe^-\leftrightarrow Li_xSi \tag{5}$$
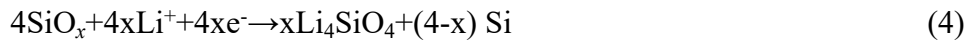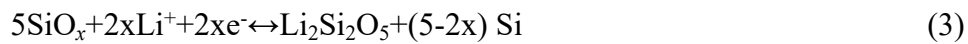
Supplementary Note 2 The CV curves at different scan rates of SCM-2.

The CV curves at different scan rates were measured to analyze lithium intercalation/deintercalation kinetics of SCM-2. As shown in Fig. S17a, the peak currents (i) in the CV curves follow a power-law relationship with the scan rate (v) as follows.

$i = av^b$

Here, a and b are adjustable parameters, log(i) is linearly dependent on log(v), and slope is b. The value of b is a kinetic factor that reveals the charge storage mechanism of the electrode. b = 0.5 represents that the charge storage of the electrode is a diffusion-controlled process, while b = 1 indicates that the charge storage is a pseudocapacitive-controlled process. The pseudocapacitive lithium storage mechanism is usually much faster than the diffusion process. Therefore, the higher the contribution of the

pseudocapacitive storage mechanism, the faster the lithium intercalation/deintercalation in the electrode material. The b values obtained by fitting the oxidation peak in Fig. S17b is 0.68, indicating that the lithium storage mechanism of SCM-2 electrode is a process controlled by both pseudocapacitance and diffusion. Furthermore, the pseudocapacitive-controlled lithium storage process was quantified using the following equation:

$$i(V) = k_1 v + k_2 v^{\frac{1}{2}} \#(1)$$

In equation (1), $k_1 v$ and $k_2 v^{1/2}$ represent the current contributions from the pseudocapacitive-controlled and diffusion-controlled processes, respectively. At a scan rate of 1.2 mV s^{-1}, the pseudocapacitive contribution reaches 67.7% (Figure S17c). At high scan rates, the pseudocapacitive-controlled mechanism enables SCM-2 to rapidly intercalate/deintercalate lithium.
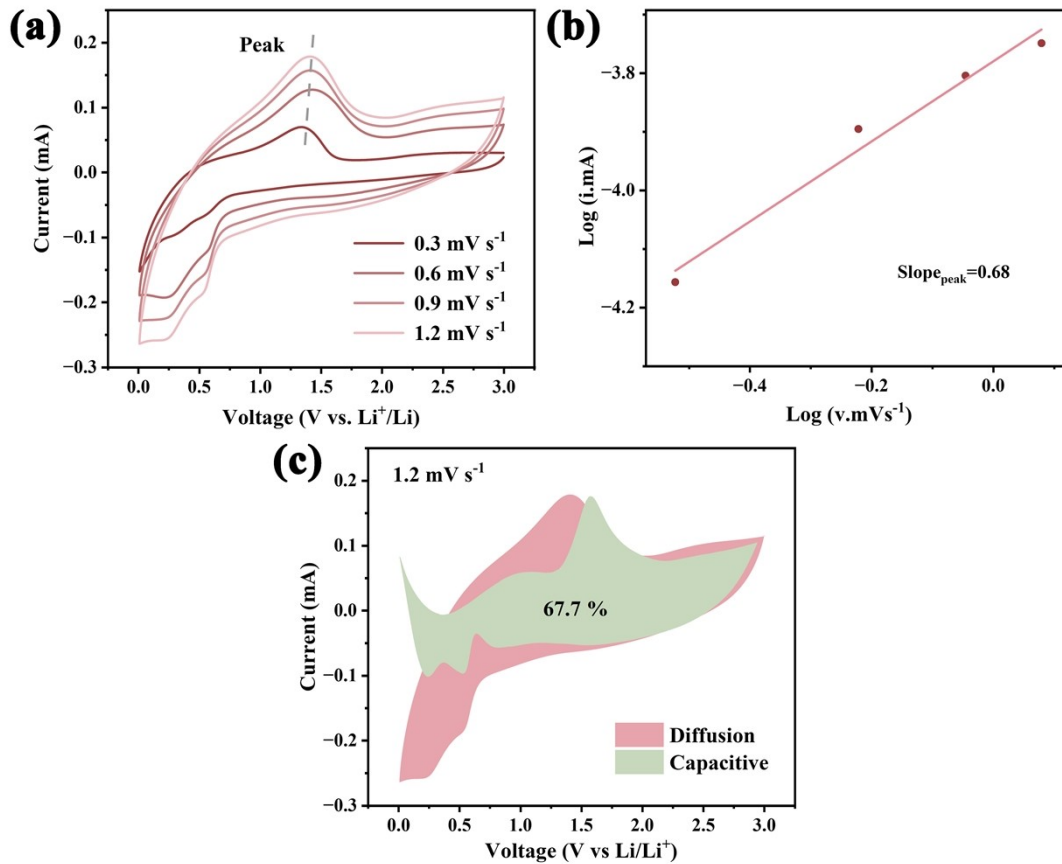
Fig. S17. (a) CV curves of SCM-2 at different scan rates from 0.3 to 1.2 mV s^{-1}. (b) log(i) versus log(v) plots of the anodic peaks (peak in (a)). (c) The capacitive contribution of SCM-2 at 1.2 mV s^{-1}.

Supplementary Note 3 A detailed study of the mutual suppression mechanism between Mn$_3$O$_4$ and SiO$_x$ was conducted using *in-situ* electrochemical impedance spectroscopy (EIS).

As shown in Fig. S17, the Nyquist data is typically composed three parts: the semi-circular in the high frequency region from SEI film resistance (R$_{SEI}$), the semi-circular in the mid frequency region from R$_{ct}$, and a linear in the low frequency region from Warburg impedance (Z$_w$). It was found that in the main discharge platform of SCM-2 (0.7 V–0.01 V), the R$_{SEI}$ and R$_{ct}$ of SCM-2 are significantly lower than those of Mn$_3$O$_4$ and SiO$_x$@C. At the same time, the R$_{SEI}$ in SCM-2 decreases as the voltage drops during the discharge process, and the R$_{ct}$ remains extremely small. The R$_{ct}$ of Mn$_3$O$_4$ shows a sudden and significant increase during the discharge process. Although it decreases at 0.7 V–0.01 V, its value remains higher than that of SCM-2. Moreover, SiO$_x$@C exhibits more severe behavior, with both R$_{SEI}$ and R$_{ct}$ increasing significantly as the voltage decreases. These phenomena also suggest that the mutual inhibition between SiO$_x$ and Mn$_3$O$_4$ can effectively suppress the volume expansion of electrode materials, thereby maintaining the stability of the SEI film. However, the comparative sample exhibits significant volume expansion, causing the SEI to become unstable and resulting in a higher impedance value.
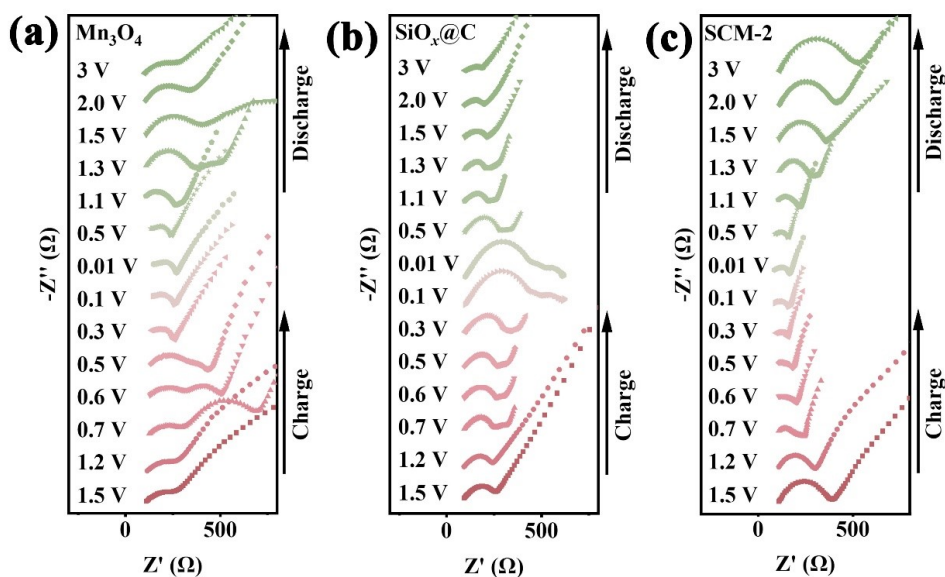
Fig. S16. *In-situ* EIS Nyquist curves for the anodes of (a) Mn_3O_4, (b)$SiO_x@C$ and (c) SCM-2 at the second cycle.

1. D.-w. Yu, Y.-l. Hou, X. Han, X.-j. Zheng, S.-j. Yu, Y.-m. Chen and X.-l. Wang, *Mater. Lett.*, 2015, **159**, 182-184.

2. J. Zhang, R. Chu, Y. Chen, Y. Zeng, Y. Zhang and H. Guo, *Electrochim. Acta*, 2019, **319**, 518-526.

3. R. Zhang, D. Wang, L.-C. Qin, G. Wen, H. Pan, Y. Zhang, N. Tian, Y. Zhou and X. Huang, *J. Mater. Chem. A*, 2017, **5**, 17001-17011.

4. W. Mao, W. Yue, Z. Xu, J. Wang, J. Zhang, D. Li, B. Zhang, S. Yang, K. Dai, G. Liu and G. Ai, *ACS Appl. Mater. Interfaces*, 2020, **12**, 39282-39292.

5. J.-G. Wang, D. Jin, R. Zhou, X. Li, X.-r. Liu, C. Shen, K. Xie, B. Li, F. Kang and B. Wei, *ACS Nano*, 2016, **10**, 6227-6234.

6. D. Zhang, G. Li, J. Fan, B. Li and L. Li, *Chem.-Eur. J.*, 2018, **24**, 9632-9638.

7. J. Shan, J.-j. Wang, Y. Zhao and J.-j. Huang, *Solid State Sci.*, 2019, **92**, 89-95.

8. L. Zhu, W. Zhang, J. Chen, L. Men, J. Zhang and Y. Zhou, *J. Colloid Interface Sci.*, 2024, **669**, 740-753.

9. J. Chen, Z. Bai, X. Li, Q. Wang, J. Du, R. Lu and X. Liu, *Ceram. Int.*, 2022, **48**, 31923-31930.

10. C.-Y. Seong, S.-K. Park, Y. Bae, S. Yoo and Y. Piao, *RSC Adv.*, 2017, **7**, 37502-37507.